crystals

MDPI

Article

Fabrication of Mesoporous V_2O_5@g-C_3N_4 Nanocomposite as Photocatalyst for Dye Degradation

Sayed M. Saleh [1,2,*], Abuzar E. A. E. Albadri [1], Mohamed Ali Ben Aissa [3] and Abueliz Modwi [3,*]

1 Department of Chemistry, College of Science, Qassim University, Buraidah 51452, Saudi Arabia
2 Chemistry Branch, Department of Science and Mathematics, Faculty of Petroleum and Mining Engineering, Suez University, Suez 43721, Egypt
3 Department of Chemistry, College of Science and Arts at Al-Rass, Qassim University, Ar-Rass 51921, Saudi Arabia
* Correspondence: e.saleh@qu.edu.sa (S.M.S.); ab.khalid@qu.edu.sa (A.M.)

Abstract: This study investigated the photocatalytic degradation of RB dye by V_2O_5@g-C_3N_4 nano-catalysts. The sonication method was utilized to create V_2O_5@g-C_3N_4 nano-catalysts. V_2O_5@g-C_3N_4 nano-catalysts were characterized using X-ray diffraction (XRD), energy dispersive spectroscopy (EDS), high-resolution electron microscopy (TEM), BET-surface area analyzer, X-ray photoelectron spectroscopy (XPS), and ultraviolet spectroscopy. In the meantime, the photocatalytic activity, pH, and photocatalyst dosage are investigated in depth to account for RB dye decolorization. The rate constant for RB dye photodegradation was 0.0517 (min^{-1}) and the decolorization rate was 93.4%. The degrading efficiency of RB dye by V_2O_5@g-C_3N_4 nanocatalysts is consistent with pseudo-first-order kinetics. The results of this study demonstrated that V_2O_5@g-C_3N_4 nanocatalysts are particularly effective at destroying dyes in water.

Keywords: V_2O_5@g-C_3N_4; nanocomposite; ultrasonic power; RB dye destruction

check for updates

Citation: Saleh, S.M.; Albadri, A.E.A.E.; Aissa, M.A.B.; Modwi, A. Fabrication of Mesoporous V_2O_5@g-C_3N_4 Nanocomposite as Photocatalyst for Dye Degradation. *Crystals* **2022**, *12*, 1766. https://doi.org/10.3390/cryst12121766

Academic Editor: Masakazu Anpo

Received: 6 November 2022
Accepted: 30 November 2022
Published: 5 December 2022

1. Introduction

Textile, paper, plastic, rubber, printing, cosmetics, leather, medicines, and food processing frequently employ a range of dyes to color their products [1–4]. By dumping dye-containing effluents into the soil and aquatic systems, these companies pollute the environment and pose a significant environmental hazard. The intense color of the dyes and pigments causes major aesthetic and ecological concerns for the acquired aquatic habitat, including the restriction of benthic photosynthesis [5,6]. For the former, human drinking water safety is directly impacted by water contamination. Among the numerous contaminants, dyes such as Rhodamine B (RB) merit special attention because of their extended emission from industries and daily use, complex degradation, and toxicity [7]. Owing to the toxicity of RB, many approaches, such as chemical degradation, physical and chemical adsorption, photocatalysis, and combinations thereof [8–14], have been utilized for its harmless treatment.

In addition, several of these colors are carcinogenic and poisonous [15,16]. To solve this problem, scientists and engineers have devised a number of physical, chemical, and biological approaches for treating effluents containing dyes [17–22]. Physical procedures include the adsorption method, coagulation-flocculation technique, membrane filtration, ion-exchange technique, and so on. Although physical methods for wastewater treatment are widely employed, they are nevertheless subject to some restrictions. For instance, the adsorption technique is slow and ineffective in treating brightly colored effluent [23]. In the case of the membrane separation method, the slow separation rate, the specific filtering need, the ultrahigh vacuum conditions, and the frequent clogging of membrane pores by organic contaminants limit its applicability to dye effluent treatment.

Graphitic carbon nitride (g-C_3N_4) nanomaterials have demonstrated excellent photocatalytic performance for water treatment in visible light [24,25]. In addition, g-C_3N_4 has several advantageous properties, such as an abundance of constituent elements, high stability, and relatively simple synthesis, making it very useful in photocatalytic dye degradation [26]. However, the high recombination rate of photogenerated electron–hole pairs and inadequate visible light absorption hindered the photocatalytic efficiency of g-C_3N_4 [27]. Numerous efforts have thus been devoted to enhancing the photocatalytic activity of g-C_3N_4 nanosheets, including constructing mesoporous structures [28], doping nonmetal [29] or metal [30] metal oxide [31], and coupling this metal oxide with other substances.

This work presents a heterojunction of V_2O_5 nanoparticles with g-C_3N_4 nanosheets as a nanocomposite for RB dye photodegradation. The nanocomposite of V_2O_5@g-C_3N_4 was synthesized using a simple sonication approach aided by methanol solvent. Compared with pure g-C_3N_4 nanosheets, the V_2O_5@g-C_3N_4 nanocomposite considerably enhanced the photocatalytic degradation activity of RB under UV/Visible light. In addition, the recyclability of the V_2O_5-g-C_3N_4 nanocomposite and the mechanism for enhancing the photocatalytic efficiency under UV/Visible light were investigated, as shown in Scheme 1.

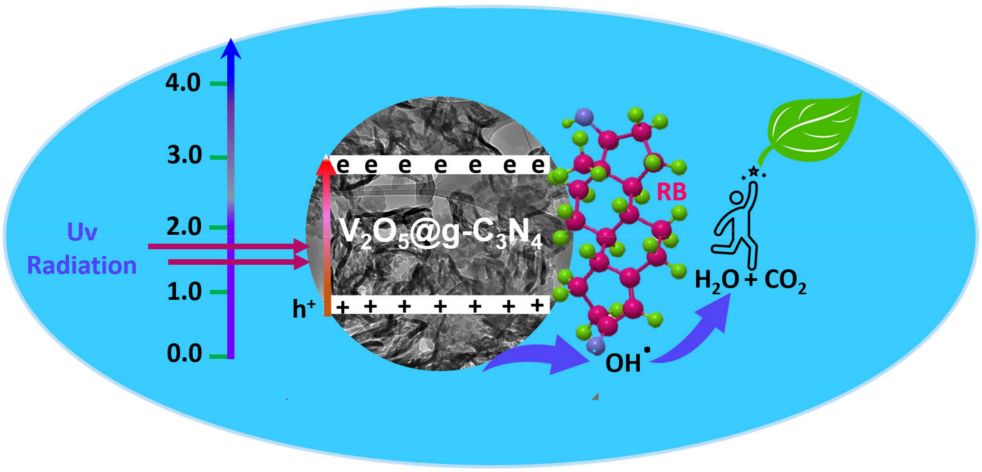

Scheme 1. Degradation of RB.

2. Materials and Methods

2.1. Nanostructures' Description Methods

Using a UV/Vis spectrophotometer in diffuse reflection mode with $BaSO_4$ as the standard, the absorbance was measured (UV-2550, Hamamatsu, Shizuoka, Japan). A Nicolet 5700 FT-IR spectrophotometer was used to record the as-prepared samples' 400–4000 cm^{-1} FT-IR spectra. The crystalline nature of the samples was investigated using a Bruker D8 Advance X-ray diffractometer (Bruker AXS, Karlsruhe, Germany) with Cu-Ka1 radiation (λ = 0.15406 nm) and a scan rate of 0.02 per second. The accelerating voltage was 40 kV, while the extraction current was 20 mA. Using ASAP 2020HD 88 equipment, the BET surface area and pore size distribution of produced samples were assessed by adsorbing N_2 at 77 K. Using a Tecnai G20 transmission electron microscope and a 200 kV accelerating voltage, the TEM pictures were captured (Hillsboro, OR, USA). For X-ray photoelectron spectroscopy (XPS), Al Ka (1486.68 eV) X-ray generators were utilized to assess the bonding characteristics of the materials (VG ESCALAB 220i-XL, West Sussex, UK). Total organic carbon (TOC) analysis (multi N/C 2100; Analytik Jena, Jena, Germany) was measured to detect the TOC values in the studied samples.

2.2. Batch Experiments

The optimum conditions of the Rhodamine B (RB) degradation process based on V_2O_5@g-C_3N_4 nanomaterials were evaluated by applying a series of degradation experiments. The influences of essential parameters on the degradation process were examined,

including RB initial concentration, the nano-catalysts' concentrations, and the investigated mediums' pH. Herein, all of the experiments were applied based on optimum conditions utilizing 0.1 L RB solution 25 ppm in a 2 mL volumetric flask. All of the measured experiments' pH values were adjusted utilizing 0.1 MHCl and 0.1 MNaOH. The examined mediums of the RB dye and V_2O_5@g-C_3N_4 nano-catalysts colloidal mixtures were performed under 4400 rpm for 10 min magnetic stirring. The UV/Vis spectra of the RB solutions were conducted using the Evolution^{TM} 200 series-Thermo Fisher Spectro-photometer (Waltham, MA, USA).

3. Results

3.1. Nanostructures' Characterizations

The optical absorption spectrum represents one of the most crucial instruments for constructing the energy band diagram. Figure 1a depicts the solid-phase absorption spectra for V_2O_5, g-C_3N_4, and V_2O_5@g-C_3N_4 nanocomposites. The absorption spectrum of V_2O_5, g-C_3N_4, and V_2O_5@g-C_3N_4 nanocomposites in the 300–800 nm wavelength range is depicted in Figure 1a. The amino absorption peak is centered at 230 nm and the strong absorption band at 320 nm indicates a conjugated carbon nitride link [32–34]. All of these peaks suggest the effective synthesis of g-C_3N_4 from urea. However, V_2O_5 nanoparticles affect and alter the peak intensity of g-C_3N_4. Compared with the pure g-C_3N_4 sample, the V_2O_5@g-C_3N_4 nanocomposites exhibit ca. in the visible light range at 400 nm.

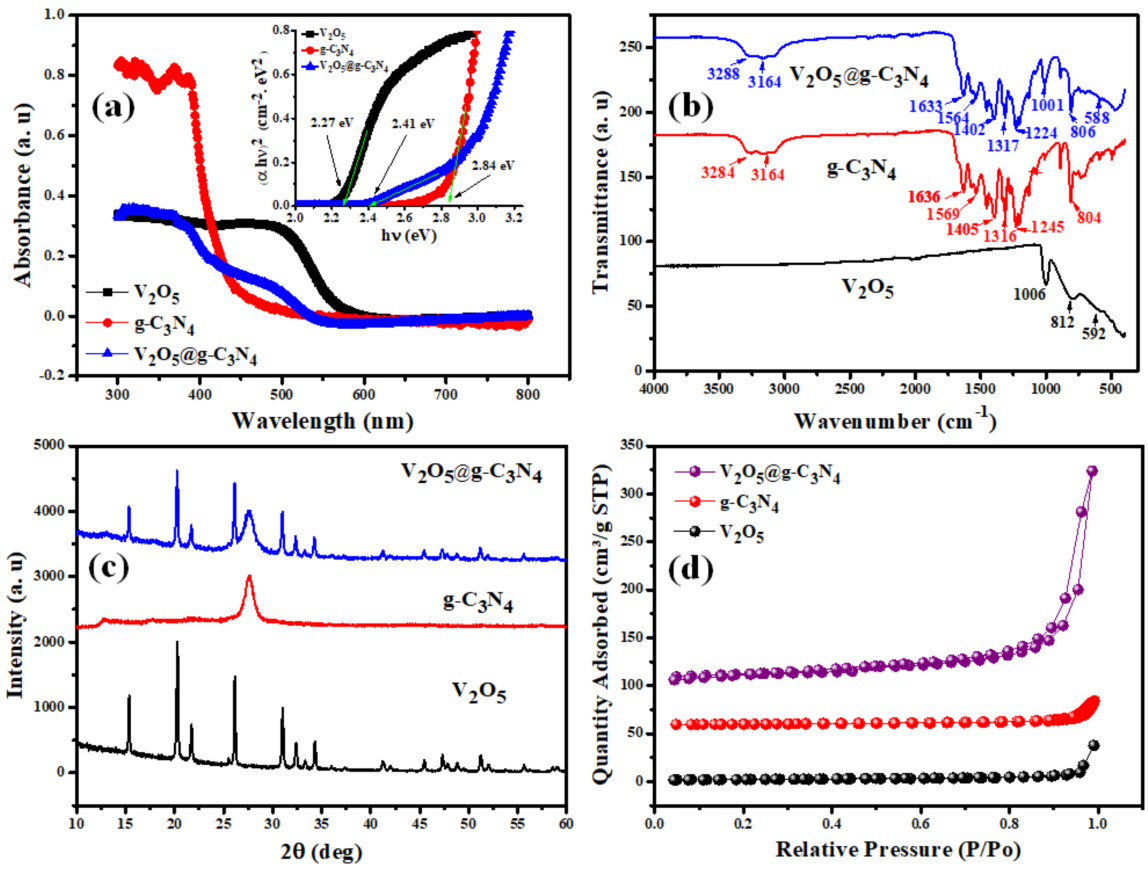

Figure 1. (**a**) UV/Vis spectra and bandgaps (in insert), (**b**) FTIR spectra, (**c**) XRD, and (**d**) nitrogen adsorption–desorption isotherm of g-C_3N_4, V_2O_5, and V_2O_5@g-C_3N_4 photocomposites.

This large absorption band peak could result from the ionizing action of g-C_3N_4 bonding. Compared with pure g-C_3N_4 nanosheets, V_2O_5@g-C_3N_4 nanocomposites exhibit the most intense broad absorption in the visible light region. The optical band gap falls from 2.84 to 2.41 eV when V_2O_5 nanoparticles are incorporated into g-C_3N_4 (see insert

in Figure 1a). The estimated and documented band gap energies of g-C_3N_4 fabricated from urea range from 2.69 to 2.88 eV, depending on several reaction circumstances, such as sintering temperature, the solvent employed, and environmental effects [35]. Xiaojuan Bai et al. informed a band gap of 2.7 eV for g-C_3N_4 nanorods [36], producing a simple reflux technique. In the same way, Sushma Rawool et al. [34] conveyed a band gap of 2.71 eV constructed by coating g-C_3N_4 nanosheets on DFNS fibers.

The FT-IR spectra of V_2O_5, g-C_3N_4, and V_2O_5@g-C_3N_4 nanocomposites are depicted in Figure 1b. In the V_2O_5 FTIR spectra, three significant absorption bands are found at 592, 812, and 1006 cm^{-1}. The bands at 592 and 812 cm^{-1} correspond to V–O–V asymmetric stretching modes, while the band at 1019 cm^{-1} is related to the V=O stretching vibration [37,38]. The characteristic band at 804 cm^{-1} in the spectra of g-C_3N_4 is attributed to out-of-plane bending modes of C–N heterocycles. The stretching vibration of C=N and aromatic C–N heterocycles corresponds to peaks at 1245, 1316, 1405, 1569, and 1636 cm^{-1} [37,39]. The spectrum of the obtained nanocomposite shows the presence of characteristic bands of g-C_3N_4 and V_2O_5, which confirms the formation of V_2O_5@g-C_3N_4.

The XRD patterns of fabricated g-C_3N_4, V_2O_5, and V_2O_5@g-C_3N_4 nanocomposites are displayed in Figure 1c. The XRD pattern of pure g-C_3N_4 shows two distinct diffraction peaks at 13.0 and 27.5° attributed to the (100) and (002) planes of carbon nitride, respectively. Based on the XRD pattern of pure V_2O_5, it was possible to guarantee that the growth of V_2O_5 would have an orthorhombic phase (JCPDS 89-0612) [40]. For the V_2O_5@g-C_3N_4 nanocomposites, both the distinctive diffraction peaks of the orthorhombic phase of V_2O_5 and g-C_3N_4 can be identified in addition to the absence of any additional impurity.

The crystallite size of the V_2O_5@g-C_3N_4 nanocomposites was computed using the Scherrer equation [41]:

$$D = \frac{0.9\lambda}{\beta cos\theta} \tag{1}$$

The expressions calculated the lattice parameters and the d-spacing:

$$d = \frac{\lambda}{2sin\theta} \tag{2}$$

$$\frac{1}{d_{hkl}} = \sqrt{\frac{h^2}{a^2} + \frac{k^2}{b^2} + \frac{l^2}{c^2}} \tag{3}$$

The crystal sizes, lattice parameters, and d-spacing of g-C_3N_4, V_2O_5, and V_2O_5@g-C_3N_4 nanocomposites are given in Table 1.

Table 1. The Eg, crystallite size, lattice parameters, pore volume, average pore diameter, and BET surface area of g-C_3N_4, V_2O_5, and V_2O_5@g-C_3N_4 photocomposites.

	V_2O_5 Nanomaterials	**Pure g-C_3N_4**	**V_2O_5@g-C_3N_4**
Energy gap (eV)	2.84	2.27	2.41
Crystallite size (nm)	45.62	44.08	44.38
Lattice parameters	a = 11.531Å, b = 4.377Å, and c = 3.564 Å	a = 6.237Å	a = 11.543Å, b = 4.382 Å, and c = 3.570 Å
d-spacing (Å)	3.88	4.74	3.96
BET surface area (m^2/g)	6.752	154	61.042
Pore volume (cm^3/g)	0.057	0.912	0.353
Pore radius (Å)	17.10	27.8	18.46

As depicted in Figure 1d, the adsorption–desorption isotherms denote a typical type IV curve per the IUPAC categorization [42,43] for all of the samples that designate mesoporous characteristic nanostructures [44]. For pure V_2O_5, the isotherm exhibits a hysteresis loop of H2 type, indicating the ink-bottle-type pore structure as typically shown by inorganic oxide [45]. Besides, g-C_3N_4 exhibits hysteresis of type H3, according to the IUPAC or

Brunauer's classification for sorption isotherms with a slit-like pre-structure. The V_2O_5@g-C_3N_4 nanocomposites display an overlap of type H2 and H3 loops, suggesting the existence of both types of pores, i.e., ink-bottle and slit-like pores [46]. This finding means that the coupling of V_2O_5 to the g-C_3N_4 has altered the hosting matrix pore size features. The BET surface area was 6.752, 154, and 61.042 $m^2.\ g^{-1}$ for V_2O_5, g-C_3N_4, and V_2O_5@g-C_3N_4 nanocomposites, respectively (Table 1). The BJH pore size distribution, derived from the desorption branch of the isotherm (Figure 1d), shows a narrow pore size distribution for g-C_3N_4 and V_2O_5@g-C_3N_4 nanocomposites (Table 1). The enhanced porosity characteristic of V_2O_5@g-C_3N_4 is revealed by the larger specific surface area. A higher pore volume will boost photocatalytic activity owing to more available active sites at the surface, facilitating charge carrier migration [47].

The morphologies and microstructures of V_2O_5, g-C_3N_4, and V_2O_5@g-C_3N_4 samples were further analyzed using transmission electron microscopy (TEM). The structure of pure g-C_3N_4 appears to be that of a nanosheet, as can be seen rather plainly in Figure 2b. Regarding the V_2O_5@g-C_3N_4 photocomposite (Figure 2c), it can be observed that a few smaller V_2O_5 nanoparticles are encased within the thin layers of g-C_3N_4. In addition, the energy-dispersive X-ray spectrometer (EDS) (Figure 2f) provided evidence that the elements in question were successfully mixed.

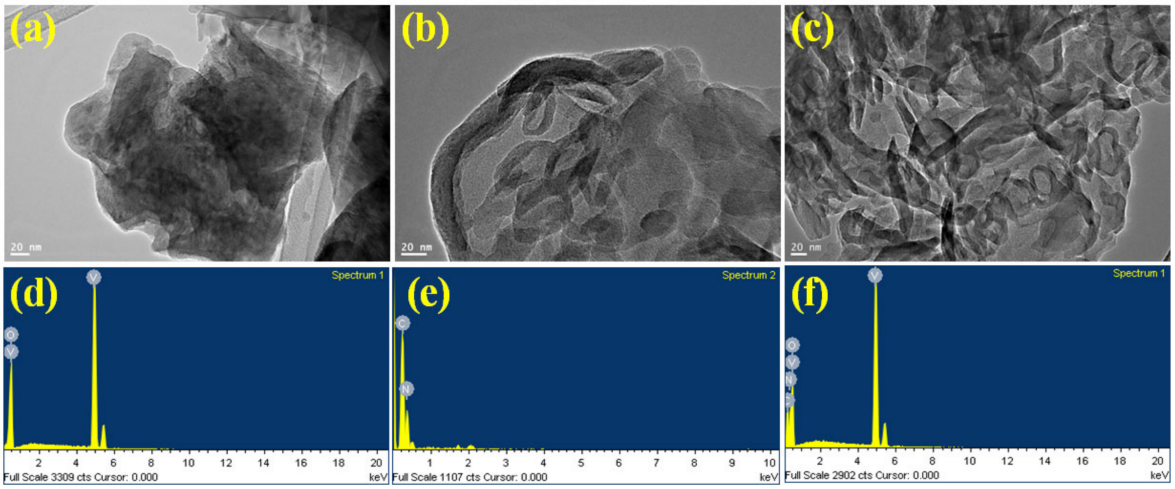

Figure 2. TEM pictures and EDX of V_2O_5 (**a**,**d**), g-C_3N_4 (**b**,**e**), and V_2O_5@g-C_3N_4 (**c**,**f**).

Figure 3 displays XPS spectral curves that can be used to determine the elemental composition, surface configuration, and oxidation states of the V_2O_5@g-C_3N_4 nanocomposite. Figure 3a shows C1s XPS spectra. Figure 3a data indicate that C–C and N=C–N with sp2-hybridized carbon are involved in constructing the created heterojunction owing to the binding energy peaks located at 284.6 eV and 285.5 eV, respectively [48]. Figure 3b depicts the XPS spectra of N1s, which exhibit two significant peaks at 395.7 eV and 397.8 eV that can be attributed to sp2-hybridized C–N and N–O, respectively [49,50]. In contrast, the XPS spectral curve of Figure 3c reveals two significant peaks at 527.1 and 528.2 eV, which could be attributed to V–O and V–OH, respectively. Therefore, the existence of V_2O5 nanoparticles' lattice oxygen in the fabricated heterojunction could be deduced [51]. V 2p XPS spectral curve underlines the presence of two peaks located at 514.6 and 527.8 eV, which may be assigned to V 2p1/2 and V 2p3/2, respectively, confirming the existence of V^{5+} in the manufactured heterostructures (Figure 3d) [52].

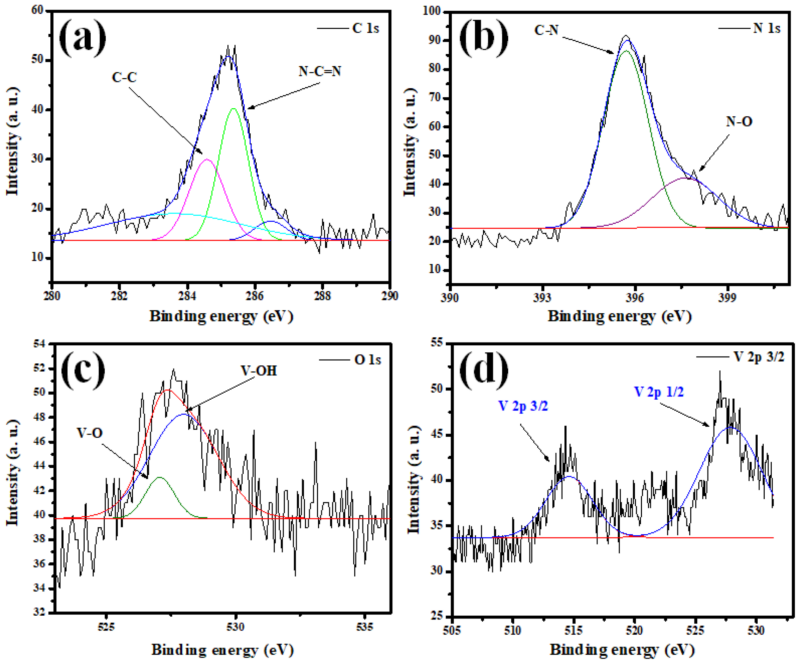

Figure 3. XPS spectra of (**a**) C-1s, (**b**) N-1s, (**c**) O-1s, and (**d**) V-2p3/2 for V_2O_5@g-C_3N_4 nanocomposite.

3.2. Photocatalysis Performance Part

3.2.1. Absorption Spectra Experiments

The Rhodamine B optical characteristics are introduced in Figure 4. The UV/Vis spectra of the RB dye present two maximum peaks at 552 and 256 nm separately. When we apply the nano-catalysts V_2O_5@g-C_3N_4 to the RB dye solutions, a substantial decrease in the prominent peaks at 552 and 256 nm is offered under UV light radiation. The spectacular absorbance spectra of the investigated RB dye depending on V_2O_5@g-C_3N_4 nano-catalysts can be attributed to the significant catalytic activity of the examined nanocomposite. Besides, the relation between the UV radiation time and the ratiometric absorbances of the RB dye was exhibited in the inset plot in Figure 5. This proves the optical activity of the V_2O_5@g-C_3N_4 nanocomposites on the degradation process of RB dye for one hour only.

Additionally, the degradation process of the RB dye was examined in the absence of UV light source radiation (in the dark). Besides, the absorbance spectra of the RB dye were collected and the resulting data give no observed changes in the absorptance spectra alteration in the absorbances of the RB dye at maxima 552 and 256 nm, correspondingly. RB shows high optical stability in the dark and in the absence of the UV radiation source [53,54], and the RB degradation process does not validate competently, as exhibited in Figure 3.

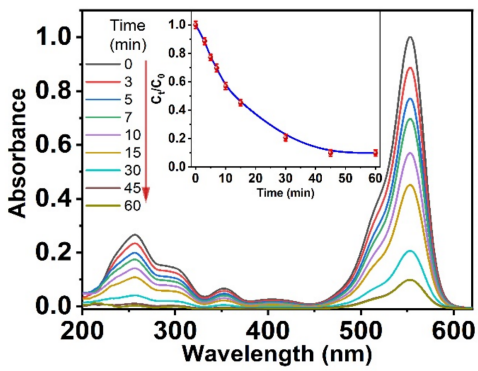

Figure 4. Absorbance spectra of Rhodamine B in the presence of V_2O_5@g-C_3N_4 photocatalyst nanoparticles.

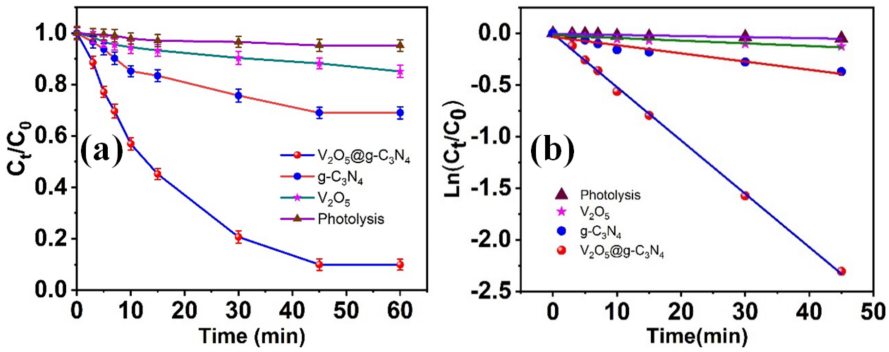

Figure 5. (**a**) The difference in photodegradation with time and (**b**) pseudo-first-order kinetics of the Rhodamine B dye.

We can observe from the obtained results that the adsorption phenomenon of the RB dye to the nano-catalysts active sites under the optimum conditions is blocked after 5 min in the presence of a constant shaking rate in the dark, while the degradation process is significantly unfunctionalized. The absorption of RB dye to the surfaces of nanomaterials was carried out in the absence of UV radiation, and the RB residues were detected at constant intervals. The obtained data exhibit a constant concentration of RB residues after 5 min. Thus, for all experiments' series, a constant shaking rate for 5 min was applied in order to obtain a regular adsorption equilibrium. The RB dye was completely degraded in the presence of V_2O_5@g-C_3N_4 under UV radiation, and the results are given in Figure 6a, where the initial concentration of the RB dye C_0 and its concentration at any time C_t are used to calculate the ratiometric values C_t/C_0, which has considerably decreased with the increasing irradiation time.

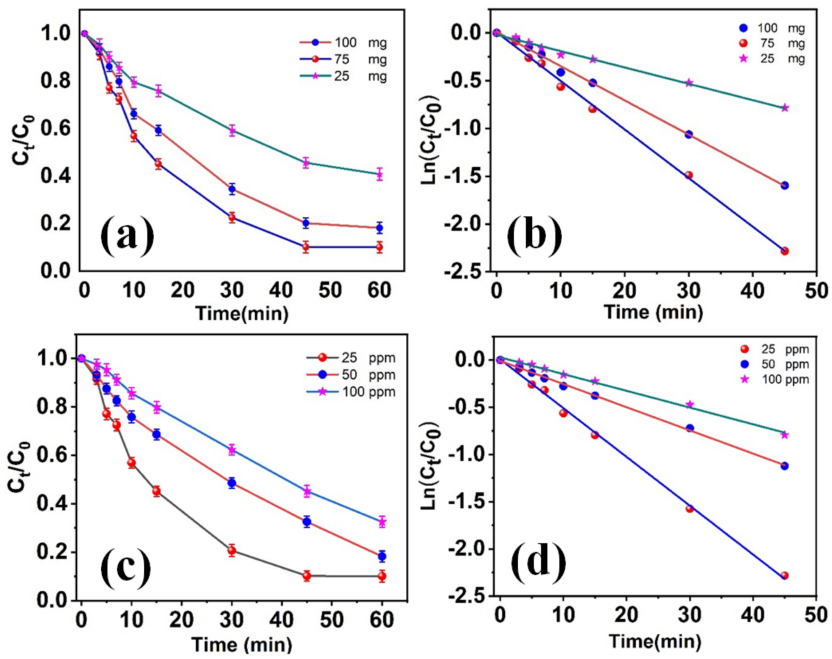

Figure 6. The photocatalytic efficiency of RB dye (**a**,**b**) at different V_2O_5@g-C_3N_4 mass concentrations and (**c**,**d**) at various RB dye concentrations.

The efficacies of the studied materials were calculated to be 31.1, 16.1, and 93.4% for g-C_3N_4, V_2O_5, and V_2O_5@g-C_3N_4, separately, demonstrating the enormous photocatalytic characteristic of the different nanomaterials including the g-C_3N_4, V_2O_5, and V_2O_5@g-C_3N_4 nano-catalysts during 60 min (Figure 5a). Moreover, the RB degradation process based on V_2O_5@g-C_3N_4 obeyed pseudo-first-order kinetics, as presented in Figure 5b. This

is because the relation of $\ln(C_0/C_t)$ versus time of UV exposure in the presence of the studied materials is expressed by the linear relationship, as shown by the strong regression (R^2). Table 2 shows that the V_2O_5@g-C_3-N_4 nanocomposite has improved photocatalytic activity owing to its high rate constant (k) and exceptionally short half-life ($t_{1/2}$). This was attributed to dye sensitization, a process in which UV excites electrons from the dye molecule's HOMO to LUMO, ejecting them into the V_2O_5 conduction band and eventually triggering dye breakdown on the semiconductor surface.

Table 2. Kinetics parameters of RB dye degradation.

Sample	K (min^{-1})	$t_{1/2}$ (min)	R^2	Degradation %	Energy Gap (ev)
g-C_3-N_4	0.0080	86.64	0.92	11.5	2.27
V_2O_5	0.0026	266.6	0.95	31.6	2.84
V_2O_5@g-C_3N_4	0.0517	13.41	0.99	93.4	2.41

3.2.2. Effect of the Nanomaterials' Dosage and RB Content on Photodegradation

The RB dye degradation process in the presence of V_2O_5@g-C_3N_4 nanocomposites was investigated by altering the nano-catalysts' concentration, as shown in Figure 6. The concentration of the V_2O_5@g-C_3N_4 nanocomposites varied within the range of 25–100 mg. The RB dye degradation process was studied in UV radiation and under optimum conditions. In the presence of 75 mg of V_2O_5@g-C_3N_4, the RB degradation process exhibited excellent efficiency after a reaction time of 1 h under UV radiation. At low concentrations of the V_2O_5@g-C_3N_4 nanocomposites, the RB particles can easily find their way to the active sites of the nano-catalysts and the destruction of these organic molecules. Moreover, the great diffusion of the tiny crystalline particles of V_2O_5@g-C_3N_4 nanomaterials enhances the probability of charge variation on the barrier region's outer surface [55].

On the other hand, at a higher concentration (100 mg) of the nano-catalysts, the diffusion of the RB dye molecules towards the active sites of the V_2O_5@g-C_3N_4 became difficult. Moreover, the agglomeration of the nano-catalysts can take place at high concentrations. This shields numerous active sites of the V_2O_5@g-C_3N_4 nano-catalysts in the degradation medium. Thus, the photons cannot achieve the nanocomposite surfaces.

To examine the concentration of the RB dye molecules in the reaction medium of the degradation process, the degradation process was studied within RB dye content within the range of 25–100 ppm under UV radiation for 1 h. The resulting data are displayed in Figure 5. The degradation process of the RB dye in the presence of V_2O_5@g-C_3N_4 nano-catalysts under UV radiation was significantly affected by the RB dye content in the reaction medium. This can be attributed to the crowding of the RB molecules in the vicinity of the active sites of the V_2O_5@g-C_3N_4 nano-catalysts, which decrease the probability of these dye molecules reaching the active sites of the nanocomposites. Regarding this explanation, the production of the hydroxyl radicals will be quenched and the efficiency of the RB degradation processes will decrease.

Moreover, overcrowding of the RB molecules at high concentrations will inhibit the UV radiation photon path that crosses the RB solution's threshold [56]. Moreover, by increasing the RB concentration, the dye molecules can adsorb the UV radiation and deactivate the degradation process considerably [57,58]. Thus, the proper concentration of the RB dye molecules was chosen to be 25 ppm for all series of experiments.

3.2.3. Effect of Inorganic Ions

The impact of cations (Ca^{2+} and Na^+) and anions (SO_4^{2-}, HCO_3^-, and Cl^-) on the photocatalytic degradation of RB was investigated. The experiments were conducted with an initial dye concentration of 25 mg L^{-1} at a solution pH of 7 and using different salts at a loading of 1 g L^{-1}. Figure 7 depicts the influence of inorganic ions on the photocatalytic degradation of RB. The % photodegradation of RB was 15.4.3%, 22.3%, 41.8%, and 53.2% in the presence of NaCl, $CaCl_2$, $NaHCO_3$, and Na_2SO_4, respectively. The presence of chloride

and sodium ions negatively influenced the photocatalytic degradation of RB among the inorganic ions.

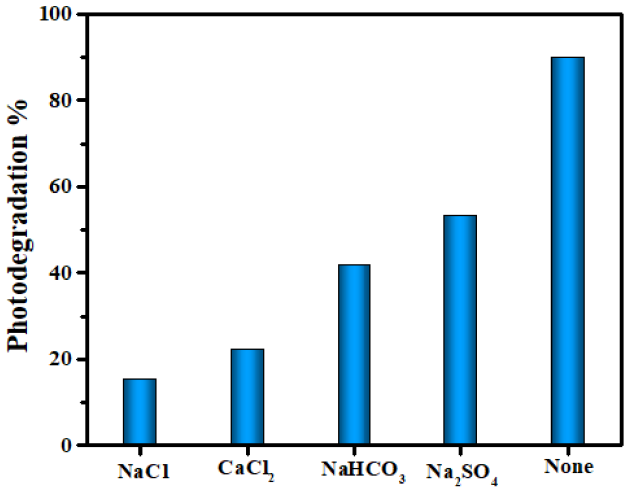

Figure 7. Effect of various salts on the photocatalytic degradation of RB.

3.2.4. pH Influence on RB Dye Degradation

To study the pH effect on the degradation process of RB on the surface of the V_2O_5@g-C_3N_4 nano-catalysts, the following experiments were conducted under optimum conditions. The RB dye molecules have a cationic form in the solution; the amine group's nitrogen atom bears a positive charge. In a basic medium, where pH is higher than 7, hydroxyl groups exist in excess, which causes an increase in the accumulation of negative charges on the nanocomposite surface. Thus, the negative charge behavior of the nano-metal oxide materials will alter into a basic surface. Thus, the efficiency of the RB degradation process will increase, as shown in Figure 8.

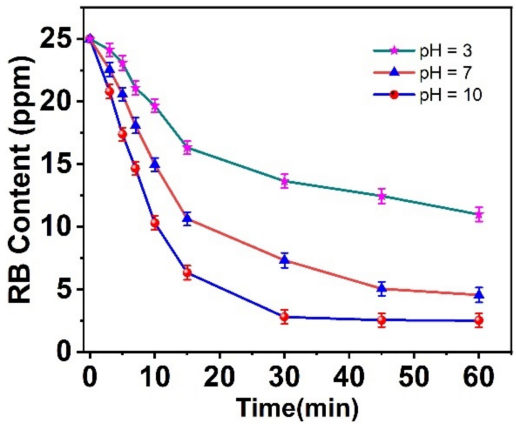

Figure 8. pH influence of RB degradation process in the presence of V_2O_5@g-C_3N_4 nano-catalysts.

On the other hand, at a lower pH of less than 7, this acidic medium will deactivate the adsorption process of RB molecules owing to the accumulation of the hydrogen protons on the surface of V_2O_5@g-C_3N_4 nano-catalysts. Remarkably, the RB degradation process initiates with the adsorption process to the surface of the nanocomposites [59]. Therefore, proficiency in the degradation processes of the organic dyes becomes significant in the basic medium [1]. The net results prove that the pH of the degradation medium is a substantial factor in the optical destruction process of the organic dye. Moreover, the acidic surface of the nanocomposites deactivates the photocatalytic process.

3.2.5. TOC Measurements

During the photocatalytic experiment, the drop in TOC (total organic carbon) concentration demonstrated that RB was mineralized and that organic carbon concentration decreased. Figure 9 depicts the experimental outcomes. C_o and C represent the initial and time-varying concentrations of TOC, respectively. The starting TOC value before irradiation was 12.53 mg/L, and the findings indicate that the concentration of TOC decreases with the increasing irradiation duration. Approximately 24% TOC removal was obtained within 80 min for the g-C_3N_4, whereas TOC removal was 64% for the V_2O_5@g-C_3N_4 system. The elimination of TOC yielded identical outcomes to those of deterioration. However, the TOC measurements revealed that total mineralization (conversion of all carbon atoms to CO or CO_2) was not possible, but complete degradation happened within 80 min. This suggests that certain organic substances (aldehydes, carboxylic acids, and so on) persisted after the chromophores (aromatic rings) had been completely shattered. In 80 min, the pH dropped from 7.21 to 6.71 during the decomposition of RB on the nanomaterials' surfaces.

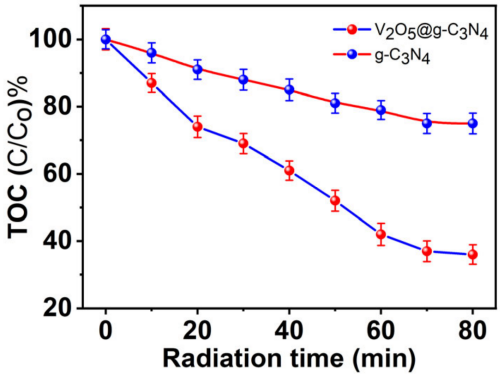

Figure 9. TOC values through the photo-degradation process.

3.2.6. Nano-Catalysts Reused Study

The ability of reused V_2O_5@g-C_3N_4 nano-catalysts for several cycles was investigated [60]. All of the experiments in this study were carried out using optimum conditions and under UV radiation. Several simple washing cycles were introduced to remove any adsorbed dyes from the surface of V_2O_5@g-C_3N_4 nano-catalysts after each degradation process and before reusing them again in further degradation processes. After four degradation process cycles, the V_2O_5@g-C_3N_4 nano-catalysts display great and stable photodegradation activity towards the RB dye, as shown in Figure 10. Moreover, the degradation process activity does not change during the four cycles experiments. The net results prove that V_2O_5@g-C_3N_4 nano-catalysts have immense stability over the degradation process.

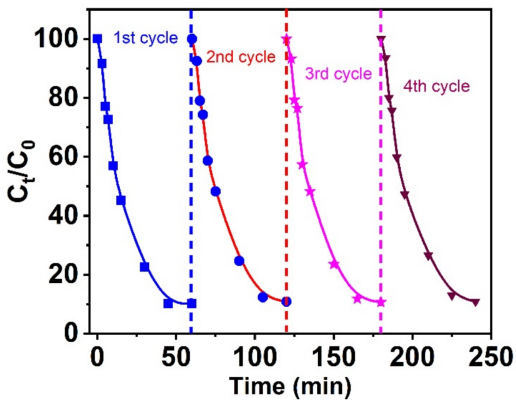

Figure 10. Photocatalytic cycling stability of V_2O_5@g-C_3N_4 photocatalyst nanoparticles.

3.2.7. Photocatalytic Mechanism

The RB degradation process in V_2O_5@g-C_3N_4 nano-catalysts is based on the free radical mechanism. This mechanism takes place extensively at the surface of the nano-catalysts. This increases the velocity of the free radical production and enhances the RB degradation process. The proposed mechanism is produced when the V_2O_5@g-C_3N_4 nanocomposites are exposed to UV radiation with a wavelength longer than the band gap between the ground state valance band and the conductance band. This process promotes the free electrons (e^-) and generates electron holes (h^+) instead of the induced electrons. To investigate the proposed degradation mechanism of RB, quenching experiments were used to explore the mechanism of photocatalytic degradation (see Figure 9). To capture e-, h+, *OH, and *O_2 in the solution, 50 mL of dye without scavenger, $AgNO_3$, EDTA, isopropanol (IPL), and ascorbic acid (ASC) was added to 50 mL of 20 mg/L of RB dye solution. In photocatalytic reactions, active compounds may be produced via several processes. Figure 11 demonstrates that the addition of EDTA and isopropanol accelerated the breakdown of RB under UV light, whereas the addition of $AgNO_3$ and ASC had little effect. The results demonstrated that the contribution of *O_2 and e^- to the photocatalytic activity was negligible, whereas *OH and h^+ played a significant role. In general, the photogenerated holes can react with water molecules to produce hydroxyl radicals, which can then react with RB molecules and break them down into CO_2 and H_2O. Likewise, photogenerated holes can directly interact with RB molecules.

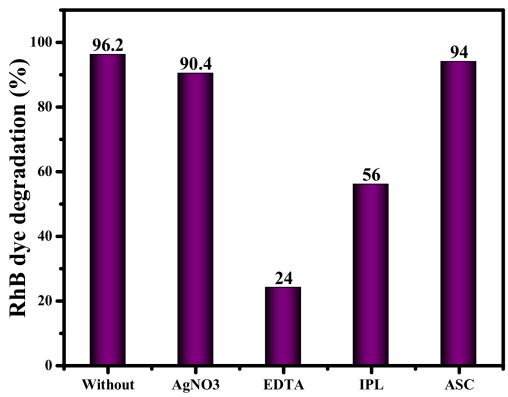

Figure 11. Quenching experiments of the proposed mechanism.

The resulting holes bear a positive charge, which attracts the adsorbed water molecules on the surface of the nano-catalysts and reacts with them to introduce OH^- radicals, which significantly impact the RB degradation process. The radicals decompose the RB organic molecules into eco-friendly smaller molecules, as exhibited in Scheme 2.

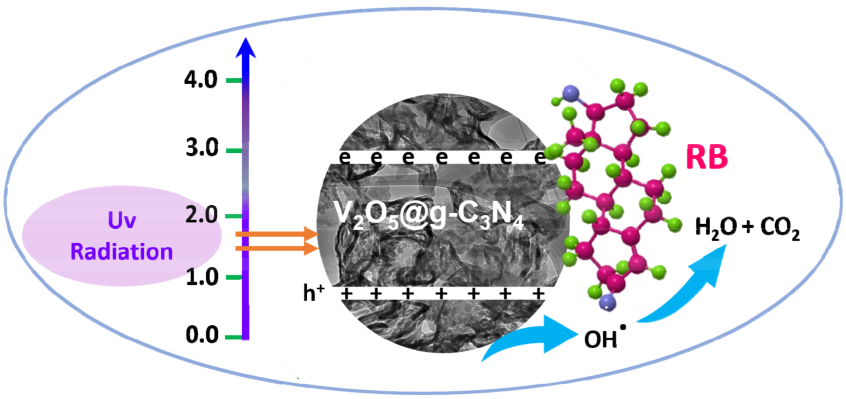

Scheme 2. The proposed mechanism of RB degradation is based on V_2O_5@g-C_3N_4 nanocomposites.

4. Conclusions

Sonication of g-C_3N_4 and V_2O_5 nanoparticles resulted in successfully constructing V_2O_5@g-C_3N_4 nano-catalyst heterojunctions. XRD peak analysis confirmed the attachment of V_2O_5 nanoparticles to g-C_3N_4 sheets by demonstrating the formation of the V_2O_5 phase alongside the characteristic g-C_3N_4 peaks. The FTIR, XRD, and XPS data showed the development of a nanocomposite with enhanced optical characteristics and smaller bandgap energy than g-C_3N_4. The photocatalytic capability of V_2O_5@g-C_3N_4 nano-catalysts was determined by RB dye degradation under visible light; the apparent reaction rate constant was seven and five times that of V_2O_5 and pure g-C_3N_4, respectively. The enhanced photocatalytic activity was attributed to the heterojunction generated by the coupling of V_2O_5 and g-C_3N_4, which enabled an efficient separation of photo-excited charge carriers.

Author Contributions: Conceptualization, S.M.S., M.A.B.A., and A.M.; methodology, A.M., S.M.S., and A.E.A.E.A.; formal analysis, S.M.S., M.A.B.A., A.E.A.E.A., and A.M.; investigation, S.M.S., M.A.B.A., A.M., and A.E.A.E.A.; resources, S.M.S., A.E.A.E.A., and A.M.; data curation, S.M.S. and A.M.; writing—original draft preparation, S.M.S., A.E.A.E.A., M.A.B.A., and A.M.; writing—review and editing, S.M.S. and A.M.; supervision, S.M.S., M.A.B.A., and A.M. All authors have read and agreed to the published version of the manuscript.

Funding: "The authors extend their appreciation to the Deputyship for Research & Innovation, Ministry of Education, Saudi Arabia for funding this research work through the project number (QU-IF-4-5- 1-31435). The authors also thank to Qassim University for technical support".

Institutional Review Board Statement: Not applicable.

Informed Consent Statement: Not applicable.

Data Availability Statement: Not applicable.

Acknowledgments: The authors extend their appreciation to the Deputyship for Research & Innovation, Ministry of Education, Saudi Arabia for funding this research work through the project number (QU-IF-4-5- 1-31435). The authors also thank to Qassim University for technical support.

Conflicts of Interest: The authors declare no conflict of interest.

References

1. Toghan, A.; Modwi, A. Boosting unprecedented indigo carmine dye photodegradation via mesoporous MgO@ g-C_3N_4 nanocomposite. *J. Photochem. Photobiol. A Chem.* **2021**, *419*, 113467. [CrossRef]
2. Hu, H.; Xin, J.H.; Hu, H.; Wang, X.; Miao, D.; Liu, Y. Synthesis and stabilization of metal nanocatalysts for reduction reactions—A review. *J. Mater. Chem. A* **2015**, *3*, 11157–11182. [CrossRef]
3. Ghosh, B.K.; Ghosh, N.N. Applications of metal nanoparticles as catalysts in cleaning dyes containing industrial effluents: A review. *J. Nanosci. Nanotechnol.* **2018**, *18*, 3735–3758. [CrossRef]
4. Gogoi, D.; Makkar, P.; Ghosh, N.N. Solar light-irradiated photocatalytic degradation of model dyes and industrial dyes by a magnetic $CoFe_2O_4$–gC_3N_4 S-scheme heterojunction photocatalyst. *ACS Omega* **2021**, *6*, 4831–4841. [CrossRef] [PubMed]
5. Manu, B.; Chaudhari, S. Anaerobic decolorisation of simulated textile wastewater containing azo dyes. *Bioresour. Technol.* **2002**, *82*, 225–231. [CrossRef]
6. Patel, R.; Suresh, S. Decolourization of azo dyes using magnesium–palladium system. *J. Hazard. Mater.* **2006**, *137*, 1729–1741. [CrossRef] [PubMed]
7. Cai, W.; Tang, J.; Shi, Y.; Wang, H.; Jiang, X. Improved in situ synthesis of heterostructured 2D/2D BiOCl/g-C_3N_4 with enhanced dye photodegradation under visible-light illumination. *ACS Omega* **2019**, *4*, 22187–22196. [CrossRef] [PubMed]
8. Zhang, J.-J.; Qi, P.; Li, J.; Zheng, X.-C.; Liu, P.; Guan, X.-X.; Zheng, G.-P. Three-dimensional Fe_2O_3–TiO_2–graphene aerogel nanocomposites with enhanced adsorption and visible light-driven photocatalytic performance in the removal of RhB dyes. *J. Ind. Eng. Chem.* **2018**, *61*, 407–415. [CrossRef]
9. Rather, M.A.; Bhat, S.A.; Pandit, S.A.; Bhat, F.A.; Rather, G.M.; Bhat, M.A. As catalytic as silver nanoparticles anchored to reduced graphene oxide: Fascinating activity of imidazolium based surface active ionic liquid for chemical degradation of rhodamine B. *Catal. Lett.* **2019**, *149*, 2195–2203. [CrossRef]
10. Sang, Y.; Cao, X.; Dai, G.; Wang, L.; Peng, Y.; Geng, B. Facile one-pot synthesis of novel hierarchical Bi_2O_3/Bi_2S_3 nanoflower photocatalyst with intrinsic pn junction for efficient photocatalytic removals of RhB and Cr (VI). *J. Hazard. Mater.* **2020**, *381*, 120942. [CrossRef]

11. Khan, M.S.; Khalid, M.; Shahid, M. A Co (II) coordination polymer derived from pentaerythritol as an efficient photocatalyst for the degradation of organic dyes. *Polyhedron* **2021**, *196*, 114984. [CrossRef]
12. Refat, M.S.; Saad, H.A.; Gobouri, A.A.; Alsawat, M.; Adam, A.M.A.; Shakya, S.; Gaber, A.; Alsuhaibani, A.M.; El-Megharbel, S.M. Synthesis and spectroscopic characterizations of nanostructured charge transfer complexes associated between moxifloxacin drug donor and metal chloride acceptors as a catalytic agent in a recycling of wastewater. *J. Mol. Liq.* **2022**, *349*, 118121. [CrossRef]
13. Alminderej, F.M.; Younis, A.M.; Albadri, A.E.; El-Sayed, W.A.; El-Ghoul, Y.; Ali, R.; Mohamed, A.M.A.; Saleh, S.M. The superior adsorption capacity of phenol from aqueous solution using Modified Date Palm Nanomaterials: A performance and kinetic study. *Arab. J. Chem.* **2022**, *15*, 104120. [CrossRef]
14. Saleh, S.; Younis, A.; Ali, R.; Elkady, E. Phenol removal from aqueous solution using amino modified silica nanoparticles. *Korean J. Chem. Eng.* **2019**, *36*, 529–539. [CrossRef]
15. Khezami, L.; Ben Aissa, M.A.; Modwi, A.; Guesmi, A.; Algethami, F.K.; Bououdina, M. Efficient removal of organic dyes by Cr-doped ZnO nanoparticles. *Biomass Convers. Biorefinery* **2022**, *2022*, 1–14. [CrossRef]
16. Modwi, A.; Khezami, L.; Ghoniem, M.G.; Nguyen-Tri, P.; Baaloudj, O.; Guesmi, A.; AlGethami, F.K.; Amer, M.S.; Assadi, A.A. Superior removal of dyes by mesoporous MgO/g-C_3N_4 fabricated through ultrasound method: Adsorption mechanism and process modeling. *Environ. Res.* **2022**, *205*, 112543. [CrossRef] [PubMed]
17. Gupta, V. Application of low-cost adsorbents for dye removal—A review. *J. Environ. Manag.* **2009**, *90*, 2313–2342. [CrossRef]
18. Ahmad, A.; Mohd-Setapar, S.H.; Chuong, C.S.; Khatoon, A.; Wani, W.A.; Kumar, R.; Rafatullah, M. Recent advances in new generation dye removal technologies: Novel search for approaches to reprocess wastewater. *RSC Adv.* **2015**, *5*, 30801–30818. [CrossRef]
19. Divyapriya, G.; Nambi, I.M.; Senthilnathan, J. Nanocatalysts in Fenton based advanced oxidation process for water and wastewater treatment. *J. Bionanosci.* **2016**, *10*, 356–368. [CrossRef]
20. Khan, M.S.; Shahid, M. Improving Water Quality Using Metal−Organic Frameworks. In *Metal-Organic Frameworks for Environmental Remediation*; American Chemical Society: New York, NY, USA, 2021; pp. 171–191.
21. Khan, M.S.; Khalid, M.; Ahmad, M.S.; Kamal, S.; Shahid, M. Effect of structural variation on enzymatic activity in tetranuclear (Cu4) clusters with defective cubane core. *J. Biomol. Struct. Dyn.* **2021**, 1–14. [CrossRef]
22. Younis, A.M.; Elkady, E.M.; Saleh, S.M. Novel eco-friendly amino-modified nanoparticles for phenol removal from aqueous solution. *Environ. Sci. Pollut. Res.* **2020**, *27*, 30694–30705. [CrossRef] [PubMed]
23. Nagpal, M.; Kakkar, R. Facile synthesis of mesoporous magnesium oxide–graphene oxide composite for efficient and highly selective adsorption of hazardous anionic dyes. *Res. Chem. Intermed.* **2020**, *46*, 2497–2521. [CrossRef]
24. Yu, Y.; Hu, X.; Li, M.; Fang, J.; Leng, C.; Zhu, X.; Xu, W.; Qin, J.; Yao, L.; Liu, Z.; et al. Constructing mesoporous Zr-doped SiO_2 onto efficient Z-scheme TiO_2/g-C_3N_4 heterojunction for antibiotic degradation via adsorption-photocatalysis and mechanism insight. *Environ. Res.* **2022**, *214*, 114189. [CrossRef]
25. Du, J.; Ma, S.; Zhang, N.; Liu, W.; Lv, M.; Ni, T.; An, Z.; Li, K.; Bai, Y. Efficient photocatalytic organic degradation and disinfection performance for Ag/$AgFeO_2$/g-C_3N_4 nanocomposites under visible-light: Insights into the photocatalysis mechanism. *Colloids Surf. A Physicochem. Eng. Asp.* **2022**, *654*, 130094. [CrossRef]
26. Huang, X.; Xu, X.; Yang, R.; Fu, X. Synergetic adsorption and photocatalysis performance of g-C_3N_4/Ce-doped MgAl-LDH in degradation of organic dye under LED visible light. *Colloids Surf. A Physicochem. Eng. Asp.* **2022**, *643*, 128738. [CrossRef]
27. Zhou, G.; Meng, L.; Ning, X.; Yin, W.; Hou, J.; Xu, Q.; Yi, J.; Wang, S.; Wang, X. Switching charge transfer of g-C_3N_4/$BiVO_4$ heterojunction from type II to Z-scheme via interfacial vacancy engineering for improved photocatalysis. *Int. J. Hydrog. Energy* **2022**, *47*, 8749–8760. [CrossRef]
28. Yang, Z.; Xing, Z.; Feng, Q.; Jiang, H.; Zhang, J.; Xiao, Y.; Li, Z.; Chen, P.; Zhou, W. Sandwich-like mesoporous graphite-like carbon nitride (Meso-g-C_3N_4)/WP/Meso-g-C_3N_4 laminated heterojunctions solar-driven photocatalysts. *J. Colloid Interface Sci.* **2020**, *568*, 255–263. [CrossRef]
29. Vellaichamy, B.; Paulmony, T. Visible light active metal-free photocatalysis: N-doped graphene covalently grafted with g-C_3N_4 for highly robust degradation of methyl orange. *Solid State Sci.* **2019**, *94*, 99–105.
30. Zhang, C.; Fu, Z.; Hong, F.; Pang, G.; Dong, T.; Zhang, Y.; Liu, G.; Dong, X.; Wang, J. Non-metal group doped g-C_3N_4 combining with BiF3: Yb3+, Er3+ upconversion nanoparticles for photocatalysis in UV–Vis–NIR region. *Colloids Surf. A Physicochem. Eng. Asp.* **2021**, *627*, 127180. [CrossRef]
31. Shen, J.-H.; Chiang, T.H.; Tsai, C.K.; Jiang, Z.W.; Horng, J.J. Mechanistic insights into hydroxyl radical formation of Cu-doped ZnO/g-C_3N_4 composite photocatalysis for enhanced degradation of ciprofloxacin under visible light: Efficiency, kinetics, products identification and toxicity evaluation. *J. Environ. Chem. Eng.* **2022**, *10*, 107352. [CrossRef]
32. Yu, X.; Yin, W.; Wang, T.; Zhang, Y. Decorating g-C_3N_4 nanosheets with Ti_3C_2 MXene nanoparticles for efficient oxygen reduction reaction. *Langmuir* **2019**, *35*, 2909–2916. [CrossRef] [PubMed]
33. Mohamed, N.A.; Ullah, H.; Safaei, J.; Ismail, A.F.; Mohamad Noh, M.F.; Soh, M.F.; Ibrahim, M.A.; Ludin, N.A.; Teridi, M.A.M. Efficient photoelectrochemical performance of γ irradiated g-C_3N_4 and its g-C_3N_4@ $BiVO_4$ heterojunction for solar water splitting. *J. Phys. Chem. C* **2019**, *123*, 9013–9026. [CrossRef]
34. Rawool, S.A.; Samanta, A.; Ajithkumar, T.G.; Kar, Y.; Polshettiwar, V. Photocatalytic hydrogen generation and CO_2 conversion using g-C_3N_4 decorated dendritic fibrous nanosilica: Role of interfaces between silica and g-C_3N_4. *ACS Appl. Energy Mater.* **2020**, *3*, 8150–8158. [CrossRef]

35. Cao, S.; Yu, J. g-C_3N_4-based photocatalysts for hydrogen generation. *J. Phys. Chem. Lett.* **2014**, *5*, 2101–2107. [CrossRef] [PubMed]
36. Bai, X.; Wang, L.; Zong, R.; Zhu, Y. Photocatalytic activity enhanced via g-C_3N_4 nanoplates to nanorods. *J. Phys. Chem. C* **2013**, *117*, 9952–9961. [CrossRef]
37. Zou, H.; Xiao, G.; Chen, K.; Peng, X. Noble metal-free V 2 O 5/gC 3 N 4 composites for selective oxidation of olefins using hydrogen peroxide as an oxidant. *Dalton Trans.* **2018**, *47*, 13565–13572. [CrossRef] [PubMed]
38. Govindarajan, D.; Uma Shankar, V.; Gopalakrishnan, R. Supercapacitor behavior and characterization of RGO anchored V2O5 nanorods. *J. Mater. Sci. Mater. Electron.* **2019**, *30*, 16142–16155. [CrossRef]
39. Khezami, L.; Aissa, M.A.B.; Modwi, A.; Ismail, M.; Guesmi, A.; Algethami, F.K.; Ticha, M.B.; Assadi, A.A.; Nguyen-Tri, P. Harmonizing the photocatalytic activity of g-C_3N_4 nanosheets by ZrO_2 stuffing: From fabrication to experimental study for the wastewater treatment. *Biochem. Eng. J.* **2022**, *182*, 108411. [CrossRef]
40. Shafique, S.; Yang, S.; Iqbal, T.; Cheng, B.; Wang, Y.; Sarwar, H.; Woldu, Y.T.; Ji, P. Improving the performance of V2O5/rGO hybrid nanocomposites for photodetector applications. *Sens. Actuators A Phys.* **2021**, *332*, 113073. [CrossRef]
41. Modwi, A.; Abbo, M.A.; Hassan, E.A.; Taha, K.K.; Khezami, L.; Houas, A. Influence of Annealing Temperature on the Properties of ZnO Synthesized Via 2.3. Dihydroxysuccinic Acid Using Flash Sol-Gel Method. *J. Ovonic Res.* **2016**, *12*, 59–66.
42. Condon, J.B. *Surface Area and Porosity Determinations by Physisorption: Measurements and Theory*; Elsevier: Amsterdam, The Netherlands, 2006.
43. Rouquerol, J.; Rouquerol, F.; Llewellyn, P.; Maurin, G.; Sing, K.S. *Adsorption by Powders and Porous Solids: Principles, Methodology and Applications*; Academic Press: Cambridge, MA, USA, 2013.
44. Xiong, G.; Luo, L.; Li, C.; Yang, X. Synthesis of mesoporous ZnO (m-ZnO) and catalytic performance of the Pd/m-ZnO catalyst for methanol steam reforming. *Energy Fuels* **2009**, *23*, 1342–1346. [CrossRef]
45. Dumeignil, F.; Sato, K.; Imamura, M.; Matsubayashi, N.; Payen, E.; Shimada, H. Modification of structural and acidic properties of sol–gel-prepared alumina powders by changing the hydrolysis ratio. *Appl. Catal. A Gen.* **2003**, *241*, 319–329. [CrossRef]
46. Hao, R.; Wang, G.; Jiang, C.; Tang, H.; Xu, Q. In situ hydrothermal synthesis of g-C_3N_4/TiO_2 heterojunction photocatalysts with high specific surface area for Rhodamine B degradation. *Appl. Surf. Sci.* **2017**, *411*, 400–410. [CrossRef]
47. Li, Y.; Lv, K.; Ho, W.; Dong, F.; Wu, X.; Xia, Y. Hybridization of rutile TiO_2 (rTiO_2) with g-C3N4 quantum dots (CN QDs): An efficient visible-light-driven Z-scheme hybridized photocatalyst. *Appl. Catal. B Environ.* **2017**, *202*, 611–619. [CrossRef]
48. Shawky, A.; Albukhari, S.M.; Amin, M.S.; Zaki, Z.I. Mesoporous V2O5/g-C_3N_4 nanocomposites for promoted mercury (II) ions reduction under visible light. *J. Inorg. Organomet. Polym. Mater.* **2021**, *31*, 4209–4221. [CrossRef]
49. Fang, S.; Xia, Y.; Lv, K.; Li, Q.; Sun, J.; Li, M. Effect of carbon-dots modification on the structure and photocatalytic activity of g-C_3N_4. *Appl. Catal. B Environ.* **2016**, *185*, 225–232. [CrossRef]
50. Ma, W.; Li, D.; Wen, B.; Ma, X.; Jiang, D.; Chen, M. Construction of novel Sr0. 4H1. 2Nb2O6·H_2O/g-C_3N_4 heterojunction with enhanced visible light photocatalytic activity for hydrogen evolution. *J. Colloid Interface Sci.* **2018**, *526*, 451–458. [CrossRef]
51. Shanmugam, M.; Alsalme, A.; Alghamdi, A.; Jayavel, R. Enhanced photocatalytic performance of the graphene-V2O5 nanocomposite in the degradation of methylene blue dye under direct sunlight. *ACS Appl. Mater. Interfaces* **2015**, *7*, 14905–14911. [CrossRef]
52. Yan, C.; Liu, L. Sn-doped V2O5 nanoparticles as catalyst for fast removal of ammonia in air via PEC and PEC-MFC. *Chem. Eng. J.* **2020**, *392*, 123738. [CrossRef]
53. Katowah, D.F.; Saleh, S.M.; Mohammed, G.I.; Alkayal, N.S.; Ali, R.; Hussein, M.A. Ultra-efficient hybrid material-based cross-linked PANI@ Cs-GO-OXS/CuO for the photocatalytic degradation of Rhodamine-B. *J. Phys. Chem. Solids* **2021**, *157*, 110208. [CrossRef]
54. Saleh, S.M. ZnO nanospheres based simple hydrothermal route for photocatalytic degradation of azo dye. *Spectrochim. Acta Part A Mol. Biomol. Spectrosc.* **2019**, *211*, 141–147. [CrossRef] [PubMed]
55. Katowah, D.F.; Saleh, S.M.; Alqarni, S.A.; Ali, R.; Mohammed, G.I.; Hussein, M.A. Network structure-based decorated CPA@ CuO hybrid nanocomposite for methyl orange environmental remediation. *Sci. Rep.* **2021**, *11*, 5056. [CrossRef]
56. Zhang, L.; Cheng, H.; Zong, R.; Zhu, Y. Photocorrosion suppression of ZnO nanoparticles via hybridization with graphite-like carbon and enhanced photocatalytic activity. *J. Phys. Chem. C* **2009**, *113*, 2368–2374. [CrossRef]
57. Ahmad, M.; Ahmed, E.; Hong, Z.L.; Ahmed, W.; Elhissi, A.; Khalid, N.R. Photocatalytic, sonocatalytic and sonophotocatalytic degradation of Rhodamine B using ZnO/CNTs composites photocatalysts. *Ultrason. Sonochemistry* **2014**, *21*, 761–773. [CrossRef]
58. Padovini, D.; Magdalena, A.; Capeli, R.; Longo, E.; Dalmaschio, C.; Chiquito, A.; Pontes, F. Synthesis and characterization of ZrO_2@ SiO_2 core-shell nanostructure as nanocatalyst: Application for environmental remediation of rhodamine B dye aqueous solution. *Mater. Chem. Phys.* **2019**, *233*, 1–8. [CrossRef]
59. Rauf, M.; Meetani, M.; Hisaindee, S. An overview on the photocatalytic degradation of azo dyes in the presence of TiO_2 doped with selective transition metals. *Desalination* **2011**, *276*, 13–27. [CrossRef]
60. Lops, C.; Ancona, A.; Di Cesare, K.; Dumontel, B.; Garino, N.; Canavese, G.; Hérnandez, S.; Cauda, V. Sonophotocatalytic degradation mechanisms of Rhodamine B dye via radicals generation by micro-and nano-particles of ZnO. *Appl. Catal. B Environ.* **2019**, *243*, 629–640. [CrossRef] [PubMed]